Tri-Band BPF with Six Transmission Zeros Based on Quad-Mode DGS Resonator and MSIR

Biao Peng[1, 2], Shufang Li[1, 2, *], and Li Deng[1, 2]

Abstract—This paper presents the comprehensive design and analysis of a tri-band bandpass filter (BPF) based on a novel quad-mode defected ground structure resonator (QMDGSR) fed by two $50\,\Omega$ microstrip lines under the source-load coupling condition. Four transmission zeros (TZs) are produced in the proposed tri-band bandpass structure with two TZs beside each passband. All the four TZs are thoroughly analysed using equivalent circuit models based on the even-/odd-mode theory, and the corresponding equation for extracting the frequency of each TZ is developed and verified. The bandwidths (BWs) of the 1st and 3rd operating bands are broadened by incorporating the proposed tri-band bandpass structure with a traditional microstrip stepped impedance resonator (MSIR). Also, two additional TZs are generated due to the coupling between the feeding lines and the newly incorporated MSIR, which significantly result in the passband selectivity improvement. The lower and upper stopband rejections of the fabricated prototype are as high as 83.3 and 43.9 dB, respectively.

1. INTRODUCTION

Modern microwave components and systems consist of defected ground structure resonators (DGSRs) as part of the high-profile bandpass filters (BPFs) design. Since the current distribution on the filter ground is mainly concentrated around the slot, slot-line resonators (SLRs) can be effectively folded to be more compact [1]. As presented in [2, 3], DGSRs were tightly embedded to design multiband BPFs with very compact sizes. The multimode SLR is another competitive candidate to design components with more resonance modes using a relatively smaller component size and is becoming increasingly popular. In [4–7], dual-mode, triple-mode, and quad-mode DGSRs were proposed to design BPFs with wide and flexibly controllable bandwidth (BW). On the other hand, the multimode stepped impedance resonator (SIR) has long been utilised to design muliband microwave filters with high performance since it was first systematically investigated in [8]; e.g., in [9–11], dual-band, tri-band, and quint-band BPFs were proposed based on a variety of specially designed multimode SIRs. Owing to the potential two layers on both top and bottom of the substrate, DGSRs can be efficiently utilised to design multiband filters. A dual-band BPF was realised by stacking two SLRs in [12]. A hybrid-coupled microstrip/slotline quad-mode resonator was proposed to design a quad-band BPF with high selectivity in [13]. As also shown in [14–16], microstrip SIRs (MSIRs) and DGSRs were incorporated to design multiband BPFs with independent microwave operating bands using the same feeding structure.

In this investigation, a novel tri-band bandpass structure is designed by feeding the quad-mode DGSR (QMDGSR) proposed in [7] with a pair of $50\,\Omega$ microstrip feeding lines under the source-load coupling condition, and yields a totally new performance, including three passbands and four transmission zeros (TZs), which are effectively analysed using equivalent circuit models based on the

* Corresponding author: Shufang Li (bupt_paper@126.com).
[1] Beijing Key Laboratory of Network System Architecture and Convergence, Beijing University of Posts and Telecommunications, Beijing, China. [2] Beijing Laboratory of Advanced Information Network, Beijing University of Posts and Telecommunications, Beijing, China.

even-/odd-mode theory. The equations to extract the frequencies of the four TZs are deduced and verified. In order to broaden the BWs of the 1st and 3rd passbands, a traditional MSIR is incorporated with the QMDGSR on the top side of the substrate, which also produces two additional TZs beside the 1st and 3rd bands, significantly improving the filter passband selectivity.

## 2. FILTER DESIGN AND ANALYSIS

2.1. Equivalent Circuits and Transmission Zeros

Figure 1 (without the MSIR) shows the layout of the proposed tri-band bandpass structure, which is designed by feeding the QMDGSR proposed in [7] with two $50\,\Omega$ microstrip feeding lines under the source-load coupling condition. However, compared with [7], a totally different transmission response is produced with three passbands and four TZs (i.e., TZ1, TZ2, TZ3, and TZ4). Based on [5, 7], the equivalent circuit model of the proposed tri-band structure is presented in Figure 2(a), where C_P and C_S relate to the coupling from the microstrip lines to the QMDGSR and the source-load coupling between the two microstrip feeding lines, respectively. The S-parameter modelling is carried out based on the 0.79 mm-thick Rogers RT/Duroid 5870 with $\epsilon_r = 2.34$ using the ADS software. The EM-/LC-simulated S-parameters shown in Figure 2(b) are in good agreement.

In order to analyse the operating mechanisms of the four TZs, transmission coefficients (S_{21}) of the tri-band bandpass structure are demonstrated in Figure 3 with different source-load coupling strengths as the parameter by adjusting the coupling distance d_2. The source-load coupling strength increases when d_2 is decreased. As presented in Figure 3, only the frequencies of TZ1 and TZ4 (i.e., f_{TZ1} and f_{TZ4}) move close to each other with the decrease of d_2, while the frequencies of TZ2 and TZ3 (i.e.,
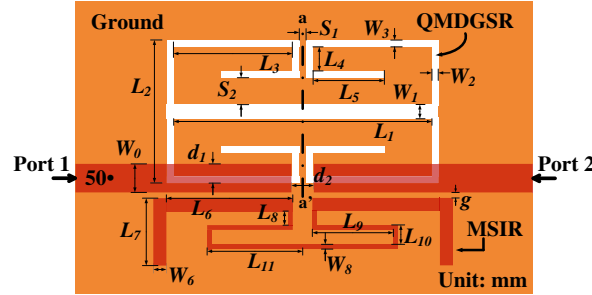

Figure 1. Layout of the proposed tri-band BPF ($W_0 = 2.34$, $W_1 = 0.68$, $W_2 = 0.3$, $W_3 = 0.3$, $W_6 = 1.0$, $W_8 = 0.4$, $L_1 = 23.5$, $L_2 = 12.0$, $L_3 = 11.05$, $L_4 = 2.8$, $L_5 = 7.3$, $L_6 = 11.4$, $L_7 = 6.4$, $L_8 = 1.5$, $L_9 = 6.5$, $L_{10} = 2.58$, $L_{11} = 7.6$, $d_1 = 1.35$, $d_2 = 1.6$, $S_1 = 0.8$, $S_2 = 2.27$, and $g = 0.3$).

(a)   (b)
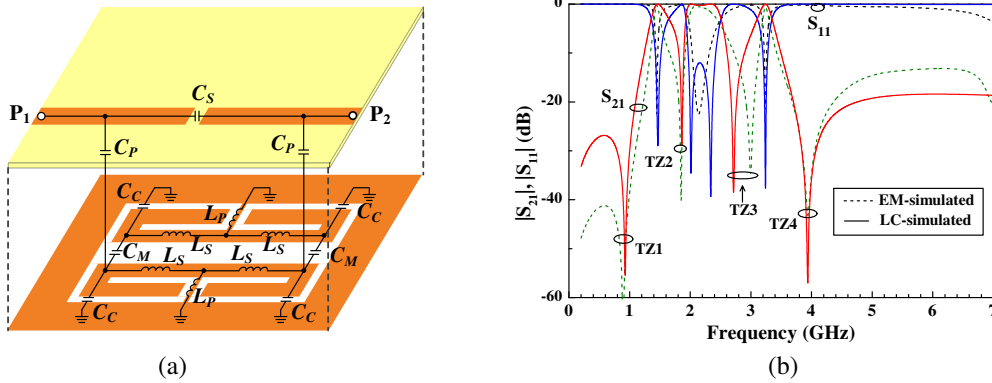
Figure 2. (a) Equivalent circuit model of the tri-band structure; (b) EM-/LC-simulated S-parameters ($C_M = 0.6\,\text{pF}$, $C_C = 1.62\,\text{pF}$, $C_P = 1.5\,\text{pF}$, $C_S = 0.2\,\text{pF}$, $L_P = 1.1\,\text{nH}$, and $L_S = 1.27\,\text{nH}$).

f_{TZ2} and f_{TZ3}) remain unchanged. It can be deduced that TZ1 and TZ4 are produced because of the source-load coupling, while TZ2 and TZ3 are due to the inherent characteristics of the proposed topology. To give a physical insight into the operating mechanisms of TZ2 and TZ3, the electric field distribution at the frequencies of f_{TZ2} and f_{TZ3} under the weakly coupling condition ($d_2 = 8.0$) are also presented in Figure 3. The difference between the electric field distribution at f_{TZ2} and f_{TZ3} can be explained based on the even-/odd-mode theory since there is a symmetric plane a-a'. At f_{TZ2}, the electric fields along the two sides of a-a' have the same density and directions, thus a-a' mostly works under the even-mode operation. Similarly, at f_{TZ3}, a-a' mostly works under the odd-mode operation. The even-/odd-mode equivalent circuit models of the QMDGSR are depicted in Figure 4(a). Under the even-mode operation, a-a' is open-circuited, which results in an inductive path ($2L_P$) running into the ground on the top of the QMDGSR; i.e., responsible for TZ2. Under the odd-mode operation, a-a' is in fact a virtual ground, and two radio frequency (RF) paths arise at the upper and lower sides of the QMDGSR. TZ3 is due to the signal counteraction between these two RF paths [17]. The current distribution at f_{TZ2} and f_{TZ3} shown in Figure 4(b) also validates this explanation. f_{TZ2} and f_{TZ3} can be calculated as shown in (3) by setting the admittances under the even-/odd-mode operations shown
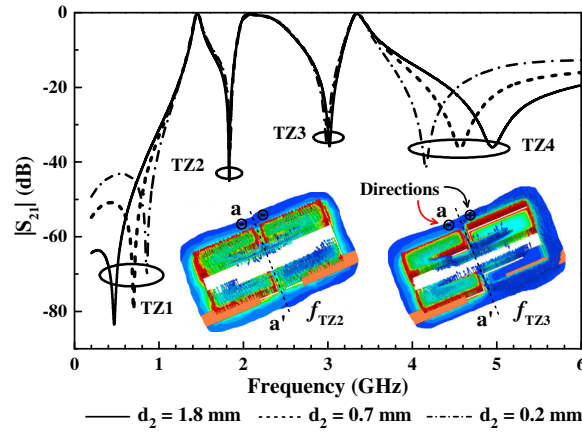
Figure 3. S_{21} of the proposed tri-band bandpass structure with different coupling strength (d_2) as the parameter and the electric field distributions under the weakly coupling condition at the frequencies of f_{TZ2} and f_{TZ3} ($d_2 = 8.0$ and $W_1 = 3.6$, based on HFSS).
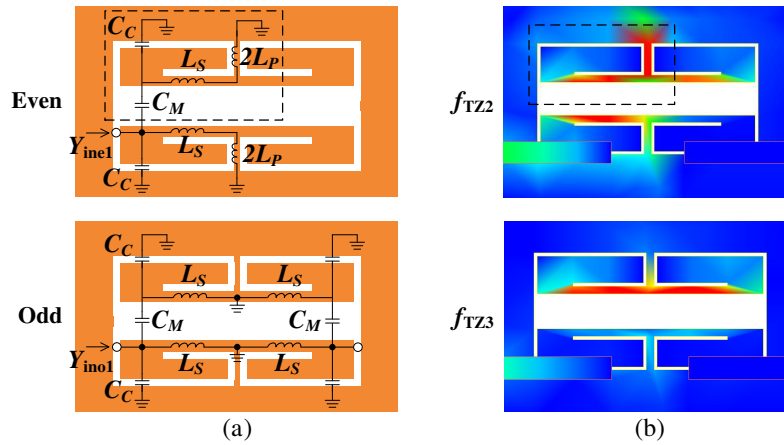
Figure 4. (a) Equivalent circuit models of the QMDGSR when a-a' is under the even-/odd-mode operations; (b) current distribution under the weakly coupling condition at the frequencies of f_{TZ2} and f_{TZ3} ($W_1 = 3.6$, based on ADS).

in (1) and (2) equal ($Y_{ine1} = Y_{ino1}$). Similarly, f_{TZ1} and f_{TZ4} can also be calculated by setting the admittances of the tri-band structure under the even-/odd-mode operations equal. However, a much more efficient method is proposed to extract f_{TZ1} and f_{TZ4} in this work.

$$Y_{ine1} = jwC_C + \frac{1}{jw(L_S + 2L_P)} + \frac{jwC_M(jwC_C + \frac{1}{jw(L_S+2L_P)})}{jwC_M + jwC_C + \frac{1}{jw(L_S+2L_P)}} \tag{1}$$

$$Y_{ino1} = jwC_C + \frac{1}{jwL_S} + \frac{jwC_M(jwC_C + \frac{1}{jwL_S})}{jwC_M + jwC_C + \frac{1}{jwL_S}} \tag{2}$$

$$f_{TZ3}, f_{TZ2} = \left\{ \frac{(C_M + C_C)(L_S + L_P) \pm \sqrt{L_P^2(C_M + C_C)^2 - L_S C_M^2(L_S + 2L_P)}}{4\pi^2(2C_M^2 + 2C_M C_C + C_C^2)L_S(L_S + 2L_P)} \right\}^{1/2} \tag{3}$$

From the LC-simulated S_{21} with different C_M as the parameter shown in Figure 5, it is clear that C_M has little effect on f_{TZ1} and f_{TZ4}. The current distribution of the tri-band bandpass structure at f_{TZ1} and f_{TZ4} are also given in Figure 5, illustrating that the current intensity mostly located on the lower-half of the QMDGSR. Hence, at the frequencies of f_{TZ1} and f_{TZ4}, the equivalent circuit model can be simplified to Figure 6(a), and the even-/odd-mode equivalent circuit models are depicted in Figure 6(b). Then, f_{TZ1} and f_{TZ4} can be calculated as shown in (4) by setting the admittances under
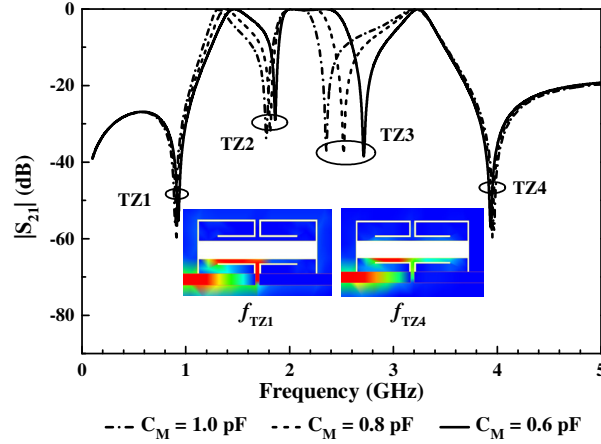
Figure 5. Effects of C_M on the four TZs; current distribution of the tri-band bandpass structure at the frequencies of f_{TZ1} and f_{TZ4} ($W_1 = 3.6$, based on ADS).
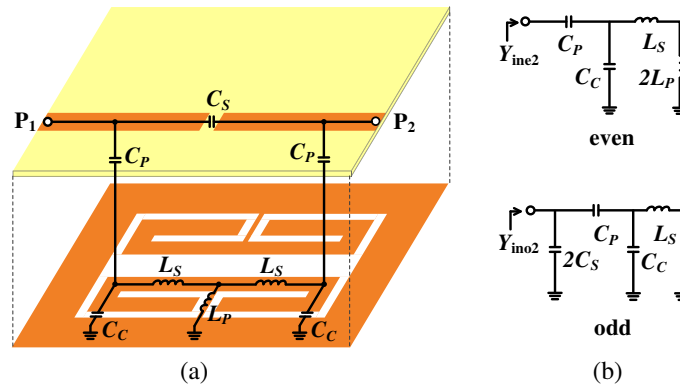
Figure 6. (a) Simplified equivalent circuit model at the frequencies of f_{TZ1} and f_{TZ4}; (b) equivalent circuit models under the even-/odd-mode operations.

the two operations equal ($Y_{ine2} = Y_{ino2}$). To verify this analysis, the simulated and calculated f_{TZ1} and f_{TZ4} are presented in Table 1 with different capacitance of C_S as the parameter, demonstrating a good agreement. The little deviation (around 5%) is due to the exclusion of the upper-half of the QMDGSR and C_M.

$$f_{TZ4}, f_{TZ1} = \left\{ \frac{2C_S(C_P + C_C)(L_S + L_P) + L_PC_P^2 \pm \sqrt{(2L_PC_S(C_P + C_C) + L_PC_P^2)^2 + 4L_PL_SC_SC_P^2(C_P + C_C)}}{8\pi^2(C_P + C_C)^2(L_S + 2L_P)L_SC_S} \right\}^{1/2} \tag{4}$$

Table 1. Comparison Between the Simulations and Calculations.

C_S (pF)	Sim. f_{TZ1} (GHz)	Cal. f_{TZ1} (GHz)	Sim. f_{TZ4} (GHz)	Cal. f_{TZ4} (GHz)
0.16	0.90	0.94	4.04	4.12
0.18	0.93	0.97	3.94	3.99
0.20	0.95	1.00	3.85	3.88

2.2. Resonance Tunability of the QMDGSR

Based on the even-/odd-mode analysis proposed in [7], frequencies of the four resonance modes of the QMDGSR (i.e., f_{m1}, f_{m2}, f_{m3}, and f_{m4}) can be calculated by Eqs. (5)–(8), and flexibly tuned by adjusting the relative dimensions. To demonstrate the tunability of the four modes, Figure 7 illustrates the S_{21} of the proposed tri-band bandpass structure under the weakly coupling condition with different dimensions as parameters. Figure 7(a) shows that f_{m1} and f_{m4} can be significantly tuned by adjusting W_1, which is due to the increase of L_S and decrease of C_C and C_M when W_1 increases. On the contrary, Figure 7(b) depicts that f_{m2} and f_{m3} are able to be effectively controlled by adjusting W_2, which is mainly because when W_2 increases, C_C would be decreased [7]. From the even-/odd-mode theory, S_1 has no effect on f_{m3} and f_{m4} under the odd-mode operation, thus it can be utilised to adjust f_{m1} and f_{m2} independently, as shown in Figure 7(c). In Figure 7(d), when L_5 increases, inductance L_S would be significantly increased, so all the four modes move to lower frequencies with the 1st mode moves much slower. As a result, f_{m2}, f_{m3}, and f_{m4} can be efficiently tuned simultaneously by adjusting L_5.

$$f_{m1} = \frac{1}{2\pi\sqrt{(L_S + 2L_P)(2C_M + C_C)}} \tag{5}$$

$$f_{m2} = \frac{1}{2\pi\sqrt{(L_S + 2L_P)C_C}} \tag{6}$$

$$f_{m3} = \frac{1}{2\pi\sqrt{L_S(2C_M + C_C)}} \tag{7}$$

$$f_{m4} = \frac{1}{2\pi\sqrt{L_SC_C}} \tag{8}$$

2.3. Tri-Band BPF Design and BW Control

Figure 1 presents the structure of the proposed tri-band BPF, which is designed by incorporating a traditional MSIR with the tri-band bandpass structure using the same feeding structure. The MSIR is bended to decrease the component size. The fundamental and 1st harmonic resonance modes of the MSIR are ustilised to provide an additional resonance mode in the 1st and 3rd passbands so as to broaden the 1st and 3rd operating BWs, respectively. Since the MSIR and the QMDGSR are located in the diagonal positions on the top and bottom of the substrate, the coupling strength between them is very weak [16]. Figure 7(c) also depicts that the 2nd resonance mode of the QMDGSR can be independently tuned while the 3rd resonance mode remain unchanged, indicating there is no cross coupling between
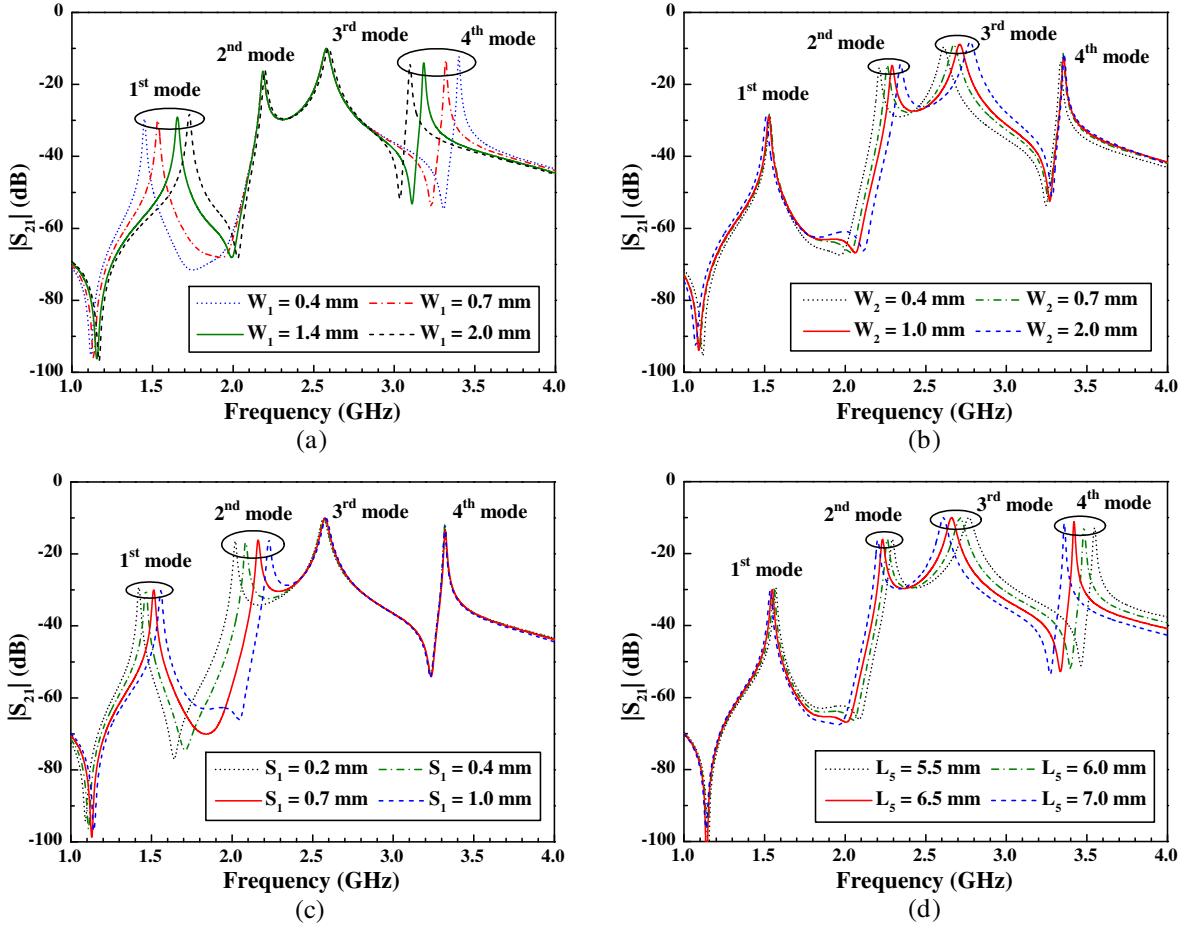
Figure 7. Transmission responses (S_{21}) of the proposed tri-band bandpass structure under the weakly coupling condition with different dimensions as parameters. (a) W_1; (b) W_2; (c) S_1; (d) L_5.

the 2nd and 3rd resonance modes of the QMDGSR.

$$\tan^2\theta_0 = K, K = Z_2/Z_1 \tag{9}$$

$$\frac{f_{R2}}{f_{R1}} = \frac{\pi}{2\tan^{-1}\sqrt{K}} \tag{10}$$

The coupling scheme of the proposed tri-band BPF is given in Figure 8(a), in which R1 denotes the fundamental resonance of the MSIR that produces the first resonance mode in the 1st passband; $R2$ denotes the 1st harmonic resonance of the MSIR that produces the second resonance mode in the 3rd passband; $m1$, $m2$, $m3$, and $m4$ denote the four resonance modes of the QMDGSR. Figure 8(b) illustrates that the external quality factor (Q_e) of the QMDGSR can be controlled by adjusting the overlap length (d_1) between the microstrip feeding lines and the QMDGSR [7]; the Q_e of the MSIR can be tuned by changing the distance (g) between the MSIR and feeding lines. Since there is no cross coupling between different resonance modes, BWs of the three passbands are mainly determined by the differences between the two resonance frequencies in each passband [5]. Figure 7 indicates that W_2 and S_1 can be well used to control the BW of the 2nd band.

The MSIR consists of two narrow and wide microstrip lines with characteristic impedances of Z_1 and Z_2, respectively. In order to simplify the design, electrical lengths of the two sections are set equal ($2\theta_0$); f_{R1} and f_{R2} can be extracted based on (9) and (10), where θ_0 is the electrical length at the frequency of f_{R1} [8]. By changing the frequency differences between the two resonance modes in the 1st and 3rd passbands, two types of tri-band BPFs are designed with narrow (Type I) and wide (Type II) 1st and 3rd passband BWs when the passband reflection coefficients (S_{11}) are better than −15 dB, as
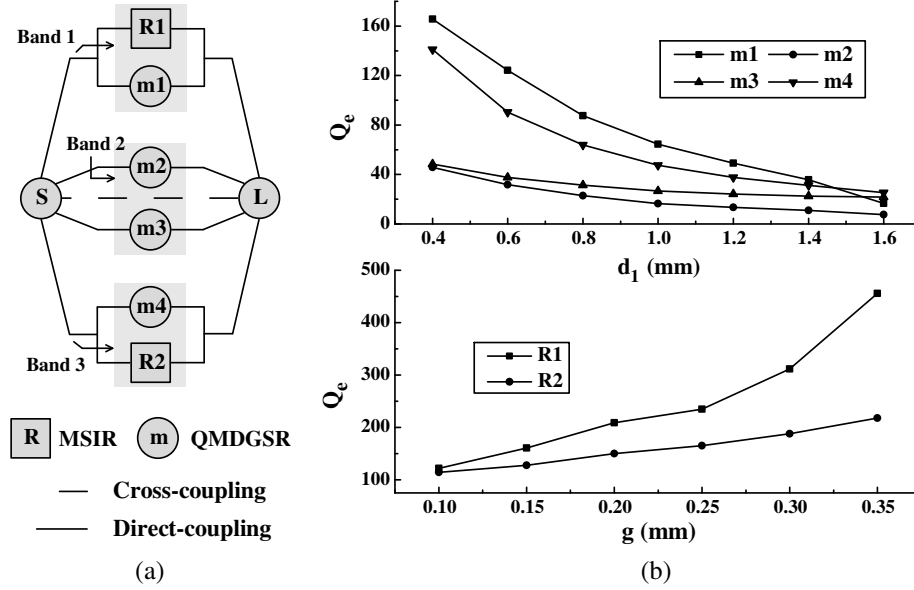
Figure 8. (a) Coupling scheme of the proposed tri-band BPF; (b) effects of d_1 and g on the Q_e of the six resonance modes.
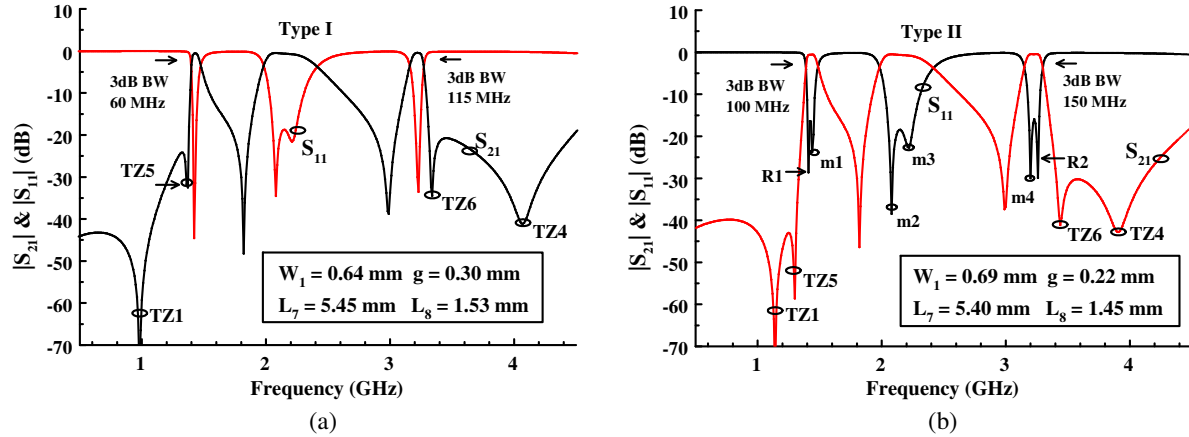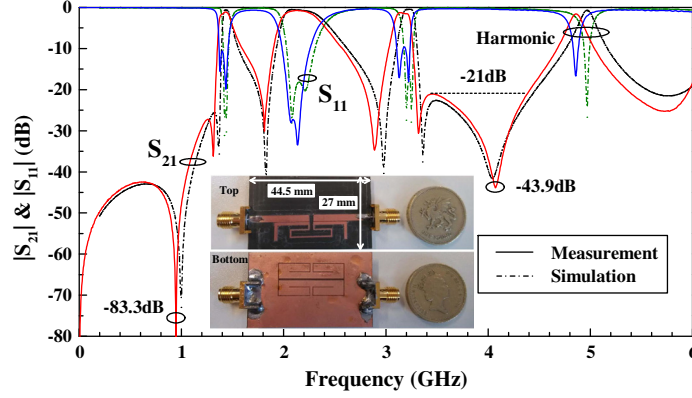

Figure 9. Simulated S-parameters of the two types of tri-band BPF with narrow (Type I) and wide (Type II) 1st and 3rd operating BWs (based on HFSS).

shown in Figure 9. It is worthwhile to mention that the BW of the second operating band is relatively wider due to the high coupling strength between the feeding lines and the two resonance modes (i.e., $m2$ and $m3$), and also due to the relatively bigger frequency difference between f_{m2} and f_{m3}. Furthermore, due to the different coupling strength between the feeding lines and the two resonance modes in the 1st and 3rd passbands (i.e., $R1$ and $m1$, $m4$ and $R2$), another two TZs (i.e., TZ5 and TZ6) are produced beside the two passbands [18], significantly improving the passband selectivity. From Figure 9, it is clear that f_{TZ5} and f_{TZ6} vary with the frequency differences between the two resonance modes in the 1st and 3rd operating bands, respectively.

3. SIMULATION AND MEASUREMENT RESULTS

The proposed tri-band BPF has been fabricated and measured; the simulations and measurements are in good agreement as presented in Figure 10. The discrepancies are mainly due to the fabrication tolerances. In the measurements, the three passbands are centred at 1.43, 2.17, and 3.16 GHz with 3 dB fractional BW (FBW) of 9.1%, 18.9%, and 5.4%, respectively. The typical insertion loss (IL) in each

Figure 10. Simulated and measured S-parameters of the fabricated tri-band BPF.

passband is 1.13, 0.74, and 1.24 dB. Due to the six TZs, the fabricated prototype performs a very good selectivity with lower and upper stopband rejections as high as 83.3 and 43.9 dB. Compared with other filters listed in Table 2, the proposed BPF exhibits competitive advantages, including: more compact size, wider BW, lower IL, and higher selectivity. Furthermore, this topology has a simple structure and much more flexible design procedure. It is worthwhile to mention that the harmonic passband around 5.0 GHz is due to the 2nd harmonic resonance of the MSIR.

Table 2. Comparison between the reference filters.

Refs.	f_0 (GHz)	FBW (%)	IL (dB)	TZs No.	Sizes (λ^2)
[2]	1.59/1.82/2.44	6.6/4.4/3.8	1.2/1.7/2.4	5	0.059×0.049
[3]	1.57/2.48/3.5	17.1/16.8/13.7	0.45/0.38/1.4	3	0.30×0.24
[12]	2.4/5.2	5.8/6.45	3.6/3.1	2	0.152×0.156
[13]	3.86/6.93/10.13/12.58	39.2/18.2/19.5/11.1	3.0/3.5/3.4/4.2	8	0.22×0.22
[14]	2.44/3.53/5.26	12.3/6.2/3.3	0.9/1.7/2.1	0	0.39×0.48
[15]	2.36/3.16	3.9/2.8	1.8/3.0	2	0.30×0.30
[16]	1.53/3.42/5.31	5.9/5.8/4.0	2.6/2.3/5.3	6	0.28×0.28
This Work	**1.43/2.17/3.16**	**9.1/18.9/5.4**	**1.13/0.74/1.24**	**6**	**0.29×0.18**

*λ is the dielectric wavelength at the central frequency of the first passband.

4. CONCLUSION

A novel tri-band bandpass structure with four TZs has been proposed by feeding a QMDGSR using two 50 Ω microstrip feeding lines under the source-load coupling condition. The operating mechanisms of the four TZs have been thoroughly analysed using equivalent circuit models based on the even-/odd-mode theory, and the corresponding equation for each TZ has been extracted and verified. The tri-band BPF has been designed by incorporating the tri-band structure with a traditional MSIR, which not only broadened the BWs of the 1st and 3rd passbands, but also produced two additional TZs. As a result, the passband selectivity of the 1st and 3rd bands has been significantly improved. The proposed topology shows competitive advantages such as compact size, low-IL, high-selectivity, and simple design procedure, which have been experimentally confirmed by a fabricated tri-band BPF prototype.

REFERENCES

1. Azadegan, R. and K. Sarabandi, "Miniature high-Q double-spiral slot-line resonator filters," *IEEE Trans. Microw. Theory Techn.*, Vol. 52, No. 5, 1548–1557, 2004.

2. Wang, L. and B. R. Guan, "Compact and high selectivity tri-band BPF using nested DDGSRs," *Electron. Lett.*, Vol. 48, No. 7, 378–379, 2012.

3. Wei, F., P. Y. Qin, Y. J. Guo, C. Ding, and X. W. Shi, "Compact balanced dual- and tri-band bpfs based on coupled complementary split-ring resonators (C-CSRR)," *IEEE Microw. Wireless Compon. Lett.*, Vol. 26, No. 2, 107–109, 2016.

4. Ebrahimi, A., W. Withayachumnankul, S. F. Al-Sarawi, and D. Abbott, "Compact dual-mode wideband filter based on complementary split-ring resonator," *IEEE Microw. Wireless Compon. Lett.*, Vol. 24, No. 3, 152–154, 2014.

5. Peng, B., S. F. Li, J. F. Zhu, Q. Y. Zhang, L. Deng, Q. S. Zeng, and Y. Gao, "Wideband bandpass filter with high selectivity based on dual-mode DGS resonator," *Microw. Opt. Tech. Lett.*, Vol. 58, No. 10, 2300–2302, 2016.

6. Liu, H. W., L. Shen, Y. Jiang, X. H., Guan, S. Wang, L. Y. Shi, and D. Ahn, "Triple-mode bandpass filter using defected ground waveguide," *Electron. Lett.*, Vol. 47, No. 6, 388–389, 2011.

7. Peng, B., S. F. Li, J. F. Zhu, Q. Y. Zhang, L. Deng, Q. S. Zeng, and Y. Gao, "Compact quad-mode bandpass filter based on quad-mode DGS resonator," *IEEE Microw. Wireless Compon. Lett.*, Vol. 26, No. 4, 234–236, 2016.

8. Mitsuo, M. and S. Yamashita, "Microstrip realization of generalized chebyshev filters with box-like coupling schemes," *IEEE Trans. Microw. Theory Tech.*, Vol. 28, No. 12, 1413–1417, 1980.

9. Peng, Y. T., L. J. Zhang, and Y. Q. Leng, "A dual-mode dual-band bandpass filter using a tri-stubs loaded multimode resonator (TSLMR)," *Journal of Electromagnetic Waves and Applications*, Vol. 28, No. 16, 2067–2073, 2014.

10. Deng, K., J. Z. Zhang, B. Wu, S. J. Sun, and X. W. Shi, "Design of microstrip tri-band bandpass filter using square ring loaded resonator," *Journal of Electromagnetic Waves and Applications*, Vol. 28, No. 18, 2364–2373, 2014.

11. Ai, J., Y. Zhang, K. D. Xu, D. Li, and Y. Fan, "Miniaturized quint-band bandpass filter based on multi-mode resonator and lambda/4 resonators with mixed electric and magnetic coupling," *IEEE Microw. Wireless Compon. Lett.*, Vol. 26, No. 5, 343–345, 2016.

12. Xu, S. S., K. X. Ma, F. Y. Meng, and K. S. Yeo, "Novel defected ground structure and two-side loading scheme for miniaturized dual-band SIW bandpass filter designs," *IEEE Microw. Wireless Compon. Lett.*, Vol. 25, No. 4, 217–219, 2015.

13. Chen, H., H. F. Zhao, K. S. Chen, Y. H. Wu, P. Tang, and H. S. Zhong, "A high selectivity quad-band bandpass filter based on hybrid-coupled microstrip/slotline quad-mode resonator," *Journal of Electromagnetic Waves and Applications*, Vol. 27, No. 15, 1902–1909, 2013.

14. Lai, X., C. H. Liang, H. Di, and B. Wu, "Design of tri-band filter based on stub loaded resonator and DGS resonator," *IEEE Microw. Wireless Compon. Lett.*, Vol. 20, No. 5, 265–267, 2010.

15. Wu, B., C. H. Liang, Q. Li, and P. Y. Qin, "Novel dual-band filter incorporating defected SIR and microstrip SIR," *IEEE Microw. Wireless Compon. Lett.*, Vol. 18, No. 6, 392–394, 2008.

16. Peng, B., S. F. Li, B. Zhang, and S. Wang, "Triband filter with high design flexibility and wide stopband using DGS and shorted stub-loaded resonator," *Microw. Opt. Tech. Lett.*, Vol. 57, No. 5, 1098–2760, 2015.

17. Rosenberg, U. and S. Amari, "Novel coupling schemes for microwave resonator filters," *IEEE Trans. Microw. Theory Tech.*, Vol. 50, No. 12, 2896–2902, 2002.

18. Liao, C. M., P. L. Chi, and C. Y. Chang, "Bandpass filters using parallel coupled stripline stepped impedance resonators," *IEEE Trans. Microw. Theory Tech.*, Vol. 55, No. 1, 147–153, 2007.